Volume 13 | Number 3 | 21 January 2017 | Pages 533–696

Soft Matter

rsc.li/soft-matter-journal

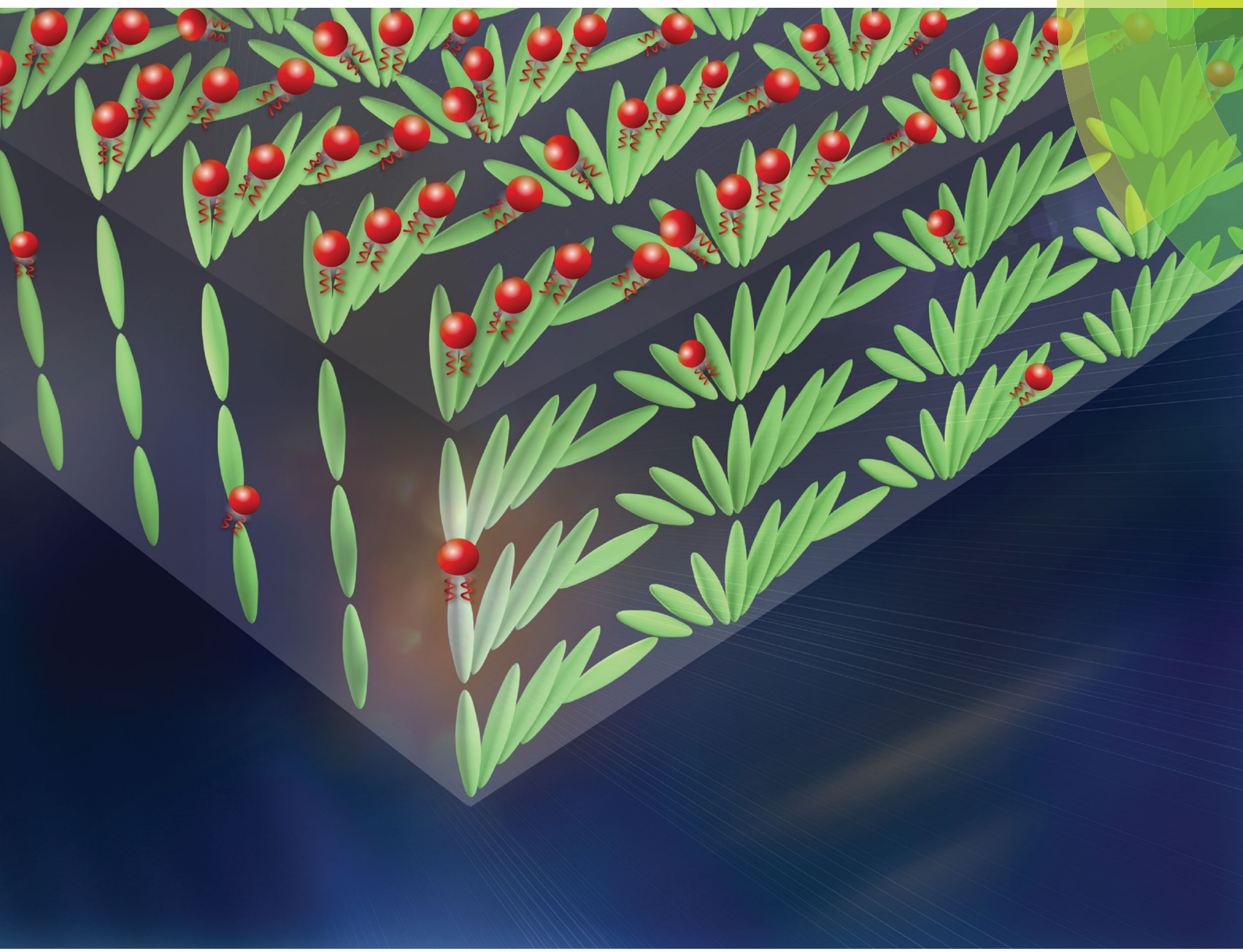

ISSN 1744-6848

ROYAL SOCIETY OF CHEMISTRY

COMMUNICATION

A. D. Rey *et al.*

Multiple-wavelength surface patterns in models of biological chiral liquid crystal membranes

Soft Matter

COMMUNICATION

View Article Online
View Journal | View Issue

Published on 08 December 2016. Downloaded by McGill University on 31/03/2017 14:42:53.

Cite this: *Soft Matter*, 2017, **13**, 541

Received 21st November 2016,
Accepted 7th December 2016

DOI: 10.1039/c6sm02619b

www.rsc.org/softmatter

Multiple-wavelength surface patterns in models of biological chiral liquid crystal membranes

P. Rofouie,[a] D. Pasini[b] and A. D. Rey*[a]

We present a model to investigate the formation of surface patterns in biological materials through the interaction of anisotropic interfacial tension, bending elasticity, and capillarity at their free surfaces. Focusing on the cholesteric liquid crystal (CLC) material model, the generalized shape equation for anisotropic interfaces using the Rapini–Papoular anchoring and Helfrich free energies is applied to understand the formation of multi-length scale patterns, such as those found in floral petals. The chiral liquid crystal-membrane model is shown to be analogous to a driven pendulum, a connection that enables generic pattern classification as a function of bending elasticity, liquid crystal chirality and anchoring strength. The unique pattern-formation mechanism emerging from the model here presented is based on the nonlinear interaction between bending-driven folding and anchoring-driven creasing. The predictions are shown to capture accurately the two-scale wrinkling of certain tulips. These new findings enable not only to establish a new paradigm for characterizing surface wrinkling in biological liquid crystals, but also to inspire the design of functional surface structures.

Chiral liquid crystals (CLCs) have been widely found in Nature and living soft materials. Biological CLCs are functional materials that display unique properties[1] and specific geometric features, such as surface wrinkles, mostly with nanoscale amplitudes and microscale single wavelength.[2] Chiral capillary pressure, known as director pressure[3] that reflects the anisotropic nature of CLC through the orientation contribution to the surface energy, has been identified as the fundamental driving force generating single-wave length surface wrinkling.[3–5] In biological membranes, these surface patterns are mostly the result of compressive strain (caused by differential swelling or constrained growth) in a stiff film resting on a compliant elastic substrate.[6–9] Moreover, surfactant-like biomolecules found in all living cells influence the elastic properties of the cell membrane, such as pulmonary surfactant which is essential to lower the surface tension in the lung and to facilitate inhalation.[10] The objective of this paper is present a theoretical model that combines membrane elasticity and liquid crystal anchoring to explain the multiple-length-scale surface wrinkles, which are widely observed in flower petals,[11] plant leaves,[12] blood cells,[13] cerebral cortex,[14] and animal living tissues.[15]

Although significant progress has been made in formulating and validating theoretical models that attempt to explain the multi-length scale surface wrinkling in biological soft materials, previous studies have been restricted to bi-layer elastic models.[8,9,13,15] There are few studies considering other chemical and biological mechanisms coupled with the compression-induced elastic deformation contributing to the wrinkling behavior[16–19] in biological surfaces and membranes. Here, to describe more complex real surfaces, we propose a physical model that includes liquid crystal anisotropy of biological materials, bending elasticity of surfactant-like biomolecules, and substrate cholesteric order; and for brevity we call it cholesteric liquid crystal membrane model (CLC-M). When the anchoring and bending effects are comparable, the surface profile may show a rich variety of multi-scale complex patterns, such as spatial period-doubling, period-tripling, and quasi-periodicity that no longer can be described by a single harmonic. In the absence of liquid crystal anchoring, the CLC-M model converges to the classical elastic membrane (M), and in the absence of an interfacial surfactant layer, it converges to the liquid crystal interface model (CLC). For a cholesteric of pitch p_0, under compression stress T_0, with surface anchoring W, and bending elasticity k_c, we find two length scales, ℓ_{chiral} and ℓ_{mem}, and two key dimensionless numbers, ω and $\bar{W}$, that control the surface morphogenesis:

$$\ell_{chiral} = \frac{2\pi}{q_0} = p_0, \quad \ell_{mem} = \frac{2\pi}{q_b} = \sqrt{\frac{k_c}{|T_0|}} \tag{1}$$

$$\omega = \frac{\ell_{chiral}}{\ell_{mem}} = \frac{p_0}{\sqrt{k_c/|T_0|}}, \quad \bar{W} = \frac{W}{T_0} \tag{2}$$

[a] *Department of Chemical Engineering, McGill University, 3610 University Street, Montreal, Quebec, H3A 2B2, Canada. E-mail: alejandro.rey@mcgill.ca*
[b] *Department of Mechanical Engineering, McGill University, 817 Sherbrook West, Montreal, Quebec, H3A 0C3, Canada*

Published on 08 December 2016. Downloaded by McGill University on 31/03/2017 14:42:53.

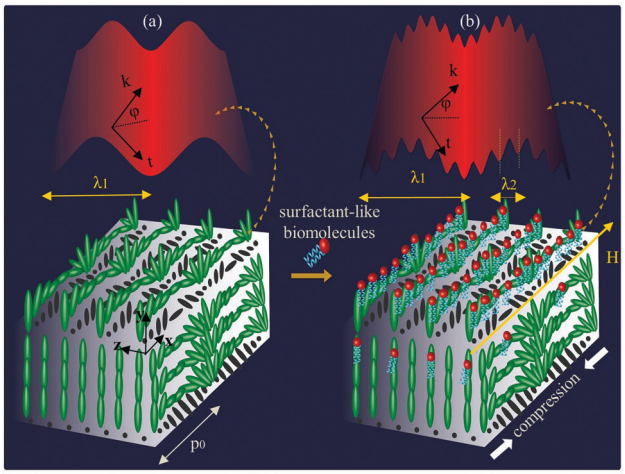

Fig. 1 Schematic of a cut of the chiral nematic membrane in the absence (a) and presence (b) of surfactants at a LC free surface. The rods in the substrate layer denote average fiber (director) orientation, the top surfaces depict the surface morphologies, the surfactant molecules are denoted by the polar head and two tails, the cholesteric axis **H** is along the "*x*" axis, the surface normal is **k**, the surface tangent is **t**, the normal angle is φ, the λ's on the top schematics denote wave-lengths, and the compression direction is "*x*".

where ω is the winding number and $\bar{W}$ is the ratio of anchoring to compression, whose magnitudes control the pattern formation mechanisms in the CLC-M model. For the limiting CLC and M models we have: CLC: $\omega \to \infty$, $\bar{W} = W/\gamma_0$, M: $\omega = 0$, $\bar{W} = 0$ and for the CLC-M complete model both ω and $\bar{W}$ are non-zero and finite; γ_0 is the isotropic surface tension, which acts as the Lagrange multiplier corresponding to the constraint of inextensibility of the membrane.[8] Schematics for the expected surface wrinkling of the CLC model and the CLC-M model are shown respectively in Fig. 1(a) and (b).

In Fig. 1(a) the cholesteric order of the substrate unwinds into a geodesic splay-bend field that interacts with the anchoring, which creates a periodic director capillary pressure that is balanced by isotropic capillarity, as reported in ref. 3 and 5. This results in a single-wave length wrinkle (top left). Here, we focus on the phenomenon shown in Fig. 1(b), where the anchoring/chirality/bending interaction creates multiple periodic scales (top right). Unwinding a helix due to surface anchoring was first considered in ref. 4.

Next we describe the essential elements of the CLC-M model. Liquid crystal orientation at the interface is defined by the director field **n**. We restrict the discussion to homeotropic anchoring ($W < 0$) and a bend and splay director field: $\mathbf{n}(x) = (\cos\theta(x), \sin\theta(x), 0)$, where the director angle, $\theta = 2\pi x/p_0$ has a domain of $[0,2\pi]$. It should be noted that the presence of a layer of surfactant-like biomolecules can change the preferred surface anchoring, and the director field.[20] The arc-length measure of the undulating surface is "s". Here we consider a single wave-vector and the amplitude of the vertical undulation is $h(x)$.

The interfacial surface tension γ for the cholesteric-elastic membrane (CLC-M) includes the anchoring energy given by Rapini and Papoular and the Helfrich free energy that describes the elasticity of membranes and surfactant–laden interfaces[21] such that:

$$\gamma = \gamma_0 + \frac{k_c}{2}\kappa^2 + \frac{W}{2}(\mathbf{n}\cdot\mathbf{k})^2 \tag{3}$$

where κ is the surface curvature. The bulk Frank elastic contribution to the shape equation due to director gradients close to the surface is assumed to be negligible. The relative importance of the bulk elastic contributions compared to anchoring energy can be evaluated by comparing the extrapolation length, $\ell_e = K/W$, (K being the Frank elastic constant) and the helix pitch p_0. For CLC-M with quite strong anchoring and large enough pitch (order of micrometers), the Frank elastic contribution is not significant as the extrapolation length is much less than the helix pitch: $\ell_e < p_0$.[22]

The generalized Cahn–Hoffman capillary vector[21,23] is the fundamental quantity that includes the curvature effects and liquid crystal orientation in one single vectorial quantity. For curved anisotropic interfaces, the bending moment tensor ($\nabla_s\cdot\mathbf{M}$) and the changes in surface tilting ($\partial\gamma(\mathbf{n},\mathbf{k})/\partial\mathbf{k}$)must be included into a generalized capillary vector. As the result, the capillary pressure includes the effects of bending ($\nabla_s^2\cdot\mathbf{M}$) and liquid crystal orientation ($\nabla_s(\partial\gamma(\mathbf{n},\mathbf{k})/\partial\mathbf{k})$).[21] The generalized capillary vector $\boldsymbol{\Xi}$ for the elastic anisotropic interface (CLC-M) has two components[21] and in the 1D model considered here it reads:

$$\begin{aligned}\boldsymbol{\Xi} &= \boldsymbol{\Xi}_\perp + \boldsymbol{\Xi}_\parallel,\\ \boldsymbol{\Xi}_\perp = \Xi_\perp\mathbf{k} = (\gamma - \mathbf{M}{:}\kappa\mathbf{tt})\mathbf{k}, \boldsymbol{\Xi}_\parallel &= \Xi_\parallel\mathbf{t} = \left(\mathbf{t}\cdot\frac{\partial\mathbf{M}}{\partial s}\right)\cdot\mathbf{tt} + \mathbf{tt}\cdot\frac{\mathrm{d}\gamma}{\mathrm{d}\mathbf{k}}\end{aligned} \tag{4}$$

The normal component $\boldsymbol{\Xi}_\perp$ describes the increase in the surface energy through dilation and the tangential component $\boldsymbol{\Xi}_\parallel$ is the change in the surface energy through rotation of the unit normal. Replacing the 1D Rapini–Papoular–Helfrich surface tension (3) in (4) yields:

$$\begin{aligned}\boldsymbol{\Xi}_\perp &= \left(\gamma_0 + \frac{W}{2}(\mathbf{n}\cdot\mathbf{k})^2 - \frac{k_c}{2}\kappa^2\right)\mathbf{k},\\ \boldsymbol{\Xi}_\parallel &= \left(k_c\frac{\partial\kappa}{\partial s} + W((\mathbf{n}\cdot\mathbf{k})(\mathbf{n}\cdot\mathbf{t}))\right)\mathbf{t}\end{aligned} \tag{5}$$

The shape equation is $\Delta P = (\nabla_s\cdot\boldsymbol{\Xi}) \equiv \mathbf{t}\cdot\partial\boldsymbol{\Xi}/\partial s$[21] where ΔP represents the pressure difference between the inner and outer sides of the cell membrane and ∇_s is the surface gradient. The capillary pressure has two contributions:

$$\mathbf{t}\cdot\frac{\partial\boldsymbol{\Xi}}{\partial s} = \frac{\partial\boldsymbol{\Xi}_\parallel}{\partial s} + \boldsymbol{\Xi}_\perp\kappa \tag{6}$$

For the current case of $\Delta P = 0$, the condition for which the capillary pressure is zero yields $\boldsymbol{\Xi} = \mathbf{C}$, where **C** is a constant vector. Considering the general case $\kappa = \kappa_0$, $\partial\kappa/\partial s = 0$, $\theta = 0$, $\varphi = \pi/2$ at $s = 0$, the constant vector is $\mathbf{C} = (\gamma_0 - (k_c/2)\kappa_0^2)\boldsymbol{\delta}_x$.

This journal is © The Royal Society of Chemistry 2017

Published on 08 December 2016. Downloaded by McGill University on 31/03/2017 14:42:53.

Introducing the compression $T_0 = (\gamma_0 - (k_c/2)\kappa_0^2)$ and replacing the curvature $\kappa = d\varphi/ds$, (6) yields:

$$k_c\frac{\partial^2\varphi}{\partial s_2} + T_0\cos\varphi + W(\mathbf{n}\cdot\mathbf{k})(\mathbf{n}\cdot\mathbf{t}) = 0 \qquad (7)$$

which is the equation of equilibrium for an elastica under a uniaxial compressive force T_0, and external anchoring force $W(\mathbf{n}\cdot\mathbf{k})(\mathbf{n}\cdot\mathbf{t})$. The thickness of biological membranes is typically 7–10 nm, which is much less than the size of the membraane.[24] Here we consider local wrinkling in a membrane with infinite length. Consequently, thin-shell approximation theory can be accounted for modeling the pattern formation in a uniform elastic liquid crystal membrane. We assume that the surface deformation does not lead to local thinning or thickening of the membrane. We are dealing with a quite strong anchoring,[4,5] $W \simeq -5 \times 10^{-5}$ J m^{-2}, and a relatively small value of the bending elasticity, $k_c \simeq 5 \times 10^{-18}$ J, which gives a micron-range bending/anchoring length, $\ell_{b/a} = \sqrt{k_c/|W|} = 0.32$ μ. To include the limiting models (CLC, M), we present in Fig. 2(a) the general morphological phase diagram of the surface patterns for a helicoidal plywood with a constant pitch, p_0 = 1.2 μm in the ternary parametric space (k_c,W,γ_0). The fundamental surface shapes at the corners of the triangle are: crease (top) with zero bending (CLC model), flat (lower right) with zero bending and zero anchoring, and fold (lower left) with zero anchoring (M model). In the triangle's interior (CLC-M model), the LC anisotropy competes with the bending elasticity, creating a range of complex surface patterns. In the interior, we can identify two main surface patterns: single wavelength and multiple wavelengths. The first is located at the limiting cases of zero anchoring/zero bending elasticity. In the absence of anchoring (the base of the triangle), the pattern corresponds to the classical compression-induced buckling of an elastic membrane.[8] With the decrease of bending elasticity, the surface patterns change into profiles with high wavenumbers, while the amplitude and the wavelength of the surface wrinkles gradually decrease and finally for the minimum value of the bending elasticity, $k_c = 10^{-19}$ J, the wrinkles almost disappear and result in the flat surface shown in the lower right corner of the ternary phase diagram. In the absence of bending elasticity (the right side of the triangle), the chirality-driven surface wrinkling is a single-wavelength periodic profile whose amplitude increases linearly with W/γ_0.[3] The multiple wavelengths pattern is observed in the regions where both bending elasticity and liquid crystal anisotropy are present. With the increase of anchoring, the surface profiles gradually change into profiles with high wavenumbers, resembling the experimentally observed multi-scale surface modulation found in the petals of the "Queen of the Night" tulip.[11] These surface patterns also reflect the two-wavelength periodic wrinkling experimentally observed at the free surface of cellulosic cholesteric liquid crystal films.[25] The wrinkling of short wavelength, $\lambda_2 \simeq 0.8$ μm, are superimposed on longer waves of length $\lambda_1 \simeq 3.5$ μm. The helix pitch and the anisotropic elastic constants of the cellulosic CLC film were suggested as the main parameters responsible for the short wavelength patterns, observed experimentally.[25]

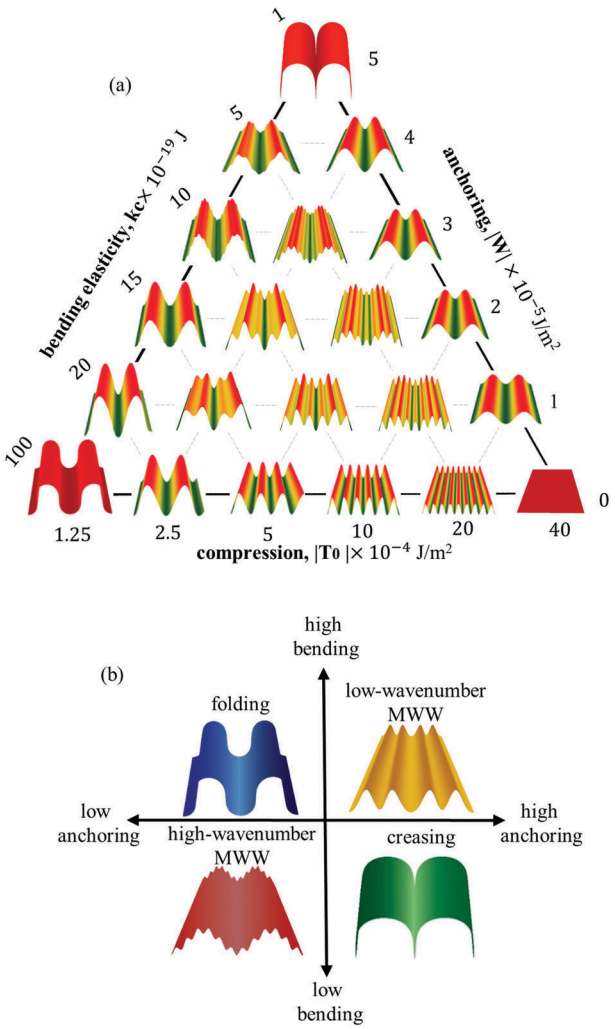

Fig. 2 (a) The ternary phase diagram of wrinkling morphologies. (b) Pattern selection depending on anchoring strength W and bending elasticity k_c. The folding appears at weak anchoring and high bending elasticity and the creasing occurs at strong anchoring and low bending elasticity. The multiple wavelengths pattern is observed where both bending elasticity and anchoring strength are comparable. MWW denotes multiple wavelength wrinkling.

An increase of the bending elasticity k_c, increases the periodicity of the smoother wrinkles and leads to the lower wavenumber. The greater the value of k_c, the greater are the amplitudes of the wrinkles. The amplitude, h, can vary from few nanometers to few microns depending on the combination of the system parameters; k_c, p_0 and W. At higher bending elasticity ($k_c \simeq 10^{-18}$ J), folding may appear. In partial summary, if the effect of the bending elasticity is predominant, the profile is a fold. If the effect of anchoring is predominant, the profile is a crease, which mostly occurs at the surface of soft materials without hard skins.[26] When both effects are comparable, the surface exhibits multiple periodic wrinkles, as illustrated in Fig. 2(b).

Next we show that the anchoring/bending/chiral model can be gainfully compared with a periodic forced pendulum, where the angular velocity of the pendulum is identical to the curvature κ of the elastic membrane. The natural frequency of the

Published on 08 December 2016. Downloaded by McGill University on 31/03/2017 14:42:53.

pendulum corresponds to the membrane wavenumber, $2\pi\sqrt{|T_0|/k_c}$ and the frequency of the external force corresponds to director wave-vector q_0. We first discuss linearized surface patterns in terms of length scales (p_0, ℓ_{mem})and anchoring ($\bar{W}$) and then describe the general case in terms of (ω,$\bar{W}$). In the pure membrane and anchoring models, the normal angle can be expressed by a single sinusoid: $\varphi_a(s) = a_1 \bar{W} p_0 \sin\left(\frac{2\pi s}{p_0}\right)$, $\varphi_b(s) = a_2 \ell_{mem} \sin\left(\frac{2\pi s}{\ell_{mem}}\right)$, respectively. In each of those two cases the system acts as a simple pendulum, with one degree of freedom (single frequency). In the presence of both anchoring and elasticity, for small amplitudes of the surface undulations, the normal angle can now be described by a linear combination of two sinusoids: $\varphi(s) = p_0(a_1\bar{W}\sin(2\pi s/p_0) + (a_2/\omega)\sin(\omega s/p_0))$. This linear approach valid for quite weak anchoring ($|\bar{W}| < 0.1$) yields the normal angle, φ, of periodic wrinkles as linear combination of two sinusoids with wave-lengths scales (p_0, p_0/ω) and amplitudes ($a_1\bar{W}p_0$, a_2p_0/ω), where $a_1 = 0.42$, and $a_2 = 0.99$.

The system can be completely described in the 3D toroidal phase (φ,κ,θ) space, where φ corresponds to the state of the pendulum, κ to the angular velocity, and θ to time. Also, the trajectories in 2D phase space (φ,κ) are identical with the pendulum limit cycles. For two different values of the helix pitch, Fig. 3(a) and (c) illustrate the surface profiles corresponding to the pure elastic membrane (M) model (no anchoring, no chirality), the anchoring/chiral (CLC) model, the anchoring/bending/chiral (CLC-M) model, and the estimated profile that is obtained by using the linear combination of the two sinusoids; the latter shows a very good agreement with the complete CLC-M model.

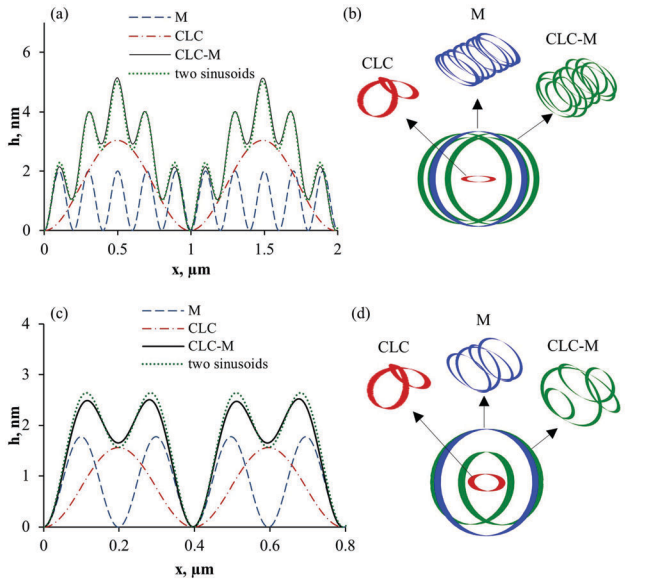

Fig. 3 Periodic surface profiles (a and c) and corresponding limit cycles (b and d) for the pure membrane (M), the pure CLC, and the elastic LC (CLC-M) models with $W = -10^{-4}$ J m^{-2}, $k_c = 5 \times 10^{-18}$ J, $T_0 = -5 \times 10^{-3}$ J m^{-2} (a and b) $P_0 = 1.98$ μm, $\omega = 10$ (c and d) $p_0 = 0.79$ μm, $\omega = 4$. h is the amplitude of the surface wrinkles. The knots above the limits cycles show the 3D (φ,κ,θ) phase portraits of the system.

For the elastic membrane model and the CLC model, the phase space is a closed curve, resembling an ellipse. In the presence of both elasticity and LC chirality, the phase space ellipse gets distorted. As illustrated in Fig. 3(b) and (d), for values of the helix pitch ($p_0 = 1.98$ & 0.79 μm), the ellipse splits into five and two cycles respectively. The dynamic analogy clearly shows that the surface pattern selection depends on the system winding number ω, or ratio between the number of times the trajectory rotates around the small cross section, and the large circumference of a torus.

Fig. 4(a) is a phase diagram in terms of pitch p_0 and bending constant k_c, and illustrates the boundary lines in which a CLC-M has an integer winding number ω; the actual multiscale periodic surface profile is shown on the bottom right. If the winding number is not an integer, the LC elastic membrane has a periodic profile but the wrinkles are not perfectly periodic (quasiperiodic). The inset clearly shows the geometric impact of increasing ω and confirms the relation between number of peaks and $p_0/2$; for $\omega = 3$ we have 3 peaks per $p_0/2$ and when $\omega = 6$ we find 6 peaks per $p_0/2$. Hence the model clearly captures the mechanism of multiple wrinkling scales as a function of the

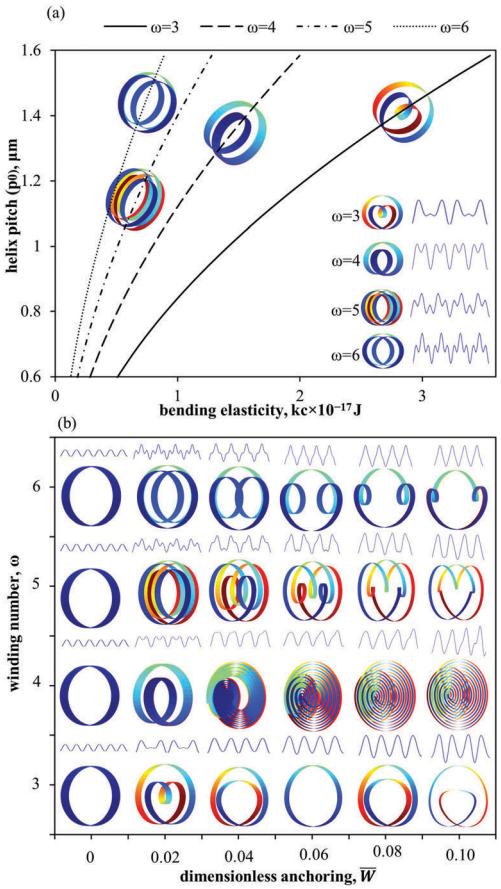

Fig. 4 Limit cycle phase diagram (a) showing the system boundaries in which the integer winding number assumes values: $\omega = 3, 4, 5, 6$. (b) Surface morphologies depending on the winding number ω and the anchoring constant $\bar{W}$. The periodic patterns on the top of the limit cycles represent the surface membrane profile.

This journal is © The Royal Society of Chemistry 2017

Published on 08 December 2016. Downloaded by McGill University on 31/03/2017 14:42:53.

magnitude of $\omega = p_0/\sqrt{k_c/|T_0|}$. As described above, the surface patterns can be characterized by ω and $\bar{W}$ and the wrinkling mode can be well characterized by limit cycles. The morphological transitions of the surface patterns are depicted in Fig. 4(b) with respect to the anchoring constant ($\bar{W}$). When the cholesteric pitch becomes short (compared to the elasticity length scale), or the anchoring strength is insignificant, the system changes to an essentially unperturbed system, thus resulting in single-wavelength periodic patterns (limit cycle is an ellipse). As the anchoring strength tends to increase, the limit cycles expand, the number of rotations decreases, and the surface structures transform into single wavelength patterns. For small winding numbers, an increase in the anchoring may result in spatial quasi-periodicity and onset of chaotic patterns (ω = 4). Not surprisingly, for weak anchoring the effect of nonlinearity is negligible and the limit cycles represent the system winding number. However, as we increase the anchoring $\bar{W}$, the nonlinearity gradually increases, thereby triggering period doubling, period tripling and other unique solutions that no longer represent the system winding number. If we increase the anchoring further ($|\bar{W}| > 0.1$), nonlinear buckling (chaotic spatial patterns) can appear.

In closing, this work presents a novel model based on the integration of liquid crystal and membrane physics, used to efficiently analyze surface pattern formation in elastic LC membranes. Through the combination of membrane elasticity and orientation gradients, we elucidate a natural setting for the creation and control of complex surface patterns. Furthermore, the morphology phase diagrams allow us to determine what characteristic pattern will appear on the surface based on the interaction of the three primitive shapes (folding, creasing, and flat). The observation of similar patterns in biological membranes can now be understood in terms of liquid crystal anisotropy and we can conclude that the numerous surface patterns observed in living tissues might be formed through LC anisotropy, similarly to the better understood case of 3D biological liquid crystal architectures. Design and fabrication of surface textures in ordered media is fundamental to the development of advanced multi-functional materials such as biosensors and actuators.

Financial support for this research was provided by Le Fonds Quebecois de la Recherche sur la Nature et les Technologies (FQRNT).

References

1 A. D. Rey, *Soft Matter*, 2010, **6**, 3402–3429.
2 I. I. Smalyukh, O. V. Zribi, J. C. Butler, O. D. Lavrentovich and G. C. L. Wong, *Phys. Rev. Lett.*, 2006, **96**, 177801.
3 P. Rofouie, D. Pasini and A. D. Rey, *Colloids Interface Sci. Commun.*, 2014, **1**, 23–26.
4 R. Meister, H. Dumoulin, M. A. Halle and P. Pieranski, *J. Phys. II*, 1996, **6**, 827–844.
5 P. Rofouie, D. Pasini and A. D. Rey, *Soft Matter*, 2015, **11**, 1127–1139.
6 L. Pocivavsek, R. Dellsy, A. Kern, S. Johnson, B. H. Lin, K. Y. C. Lee and E. Cerda, *Science*, 2008, **320**, 912–916.
7 H. Schwartz, Y. Harel and S. Efrima, *Langmuir*, 2001, **17**, 3884–3892.
8 F. Brau, H. Vandeparre, A. Sabbah, C. Poulard, A. Boudaoud and P. Damman, *Nat. Phys.*, 2011, **7**, 56–60.
9 Q. M. Wang and X. H. Zhao, *Sci. Rep.*, 2015, **5**, 31110.
10 J. Goerke, *Biochim. Biophys. Acta, Mol. Basis Dis.*, 1998, **1408**, 79–89.
11 H. M. Whitney, M. Kolle, P. Andrew, L. Chittka, U. Steiner and B. J. Glover, *Science*, 2009, **323**, 130–133.
12 E. Sharon, B. Roman, M. Marder, G. S. Shin and H. L. Swinney, *Nature*, 2002, **419**, 579.
13 L. F. Wang, C. E. Castro and M. C. Boyce, *Soft Matter*, 2011, **7**, 11319–11324.
14 T. Tallinen, J. S. Biggins and L. Mahadevan, *Phys. Rev. Lett.*, 2013, **110**, 024302.
15 A. E. Shyer, T. Tallinen, N. L. Nerurkar, Z. Y. Wei, E. S. Gil, D. L. Kaplan, C. J. Tabin and L. Mahadevan, *Science*, 2013, **342**, 212–218.
16 O. V. Manyuhina, A. M. Cazabat and M. Ben Amar, *EPL*, 2010, **92**, 16005.
17 O. V. Manyuhina, D. Mayett and J. M. Schwarz, *New J. Phys.*, 2014, **16**, 123058.
18 D. A. Beller, M. A. Gharbi, A. Honglawan, K. J. Stebe, S. Yang and R. D. Kamien, *Phys. Rev. X*, 2013, **3**, 041026.
19 T. J. White and D. J. Broer, *Nat. Mater.*, 2015, **14**, 1087–1098.
20 Y. Q. Bai and N. L. Abbott, *Langmuir*, 2011, **27**, 5719–5738.
21 A. D. Rey, *Langmuir*, 2006, **22**, 219–228.
22 P. Rofouie, D. Pasini and A. D. Rey, *J. Chem. Phys.*, 2015, **143**, 114701.
23 D. W. Hoffman and J. W. Cahn, *Surf. Sci.*, 1972, **31**, 368–388.
24 R. Hine and Facts on File Inc., *The Facts on File dictionary of biology*, Facts on File, New York, 4th edn, 2005.
25 S. N. Fernandes, Y. Geng, S. Vignolini, B. J. Glover, A. C. Trindade, J. P. Canejo, P. L. Almeida, P. Brogueira and M. H. Godinho, *Macromol. Chem. Phys.*, 2013, **214**, 25–32.
26 E. Hohlfeld and L. Mahadevan, *Phys. Rev. Lett.*, 2011, **106**, 105702.